PNAS RESEARCH ARTICLE | APPLIED PHYSICAL SCIENCES

Geometric control of topological dynamics in a singing saw

Suraj Shankar[a,1], Petur Bryde[b,1], and L. Mahadevan[a,b,c,2]

Edited by Vincenzo Vitelli, University of Chicago, Chicago, IL; received September 19, 2021; accepted March 3, 2022, by Editorial Board Member Paul Chaikin

The common handsaw can be converted into a bowed musical instrument capable of producing exquisitely sustained notes when its blade is appropriately bent. Acoustic modes localized at an inflection point are known to underlie the saw's sonorous quality, yet the origin of localization has remained mysterious. Here we uncover a topological basis for the existence of localized modes that relies on and is protected by spatial curvature. By combining experimental demonstrations, theory, and computation, we show how spatial variations in blade curvature control the localization of these trapped states, allowing the saw to function as a geometrically tunable high-quality oscillator. Our work establishes an unexpected connection between the dynamics of thin shells and topological insulators and offers a robust principle to design high-quality resonators across scales, from macroscopic instruments to nanoscale devices, simply through geometry.

musical acoustics | topological insulators | thin elastic shells

Significance

The ability to sustain notes or vibrations underlies the design of most acoustic devices, ranging from musical instruments to nanomechanical resonators. Inspired by the singing saw that acquires its musical quality from its blade being unusually bent, we ask how geometry can be used to trap and insulate acoustic modes from dissipative decay in a continuum elastic medium. By using experiments and theoretical and numerical analysis, we demonstrate that spatially varying curvature in a thin shell can localize topologically protected modes at inflection lines, akin to exotic edge states in topological insulators. A key feature is the ability to geometrically control both spatial localization and the dynamics of oscillations in thin shells. Our work uncovers an unusual mechanism for designing robust, yet reconfigurable, high-quality resonators across scales.

Musical instruments, even those made from everyday objects such as sticks, saws, pans, and bowls (1), must have the ability to create sustained notes for them to be effective. While this ability is often built into the design of the instruments, the musical saw, used to make music across the world for over a century and a half (2), is unusual in that it is just a carpenter's saw but held in an unconventional manner to allow it to sing. When a saw (Fig. 1*A*) is either bowed or struck by a mallet, it produces a sustained sound that mimics a "soprano's lyric trill" (3). Importantly, for such a note to be produced, the blade cannot be flat or bent into a J shape (Fig. 1*B*) but must be bent into an S shape (Fig. 1*C*). This geometric transformation allows the saw to sing and is well known to musicians who describe the presence of a "sweet spot," i.e., the inflection curve in the S-shaped blade; bowing near it produces the clearest notes, while bowing far from it causes the saw to fall silent (3). Early works (4, 5), including notably Scott and Woodhouse (6), attempted to understand this peculiar feature by analyzing the linearized vibrational modes of a thin elastic shell (7, 8). Through a simplified asymptotic analysis, they showed that a localized vibrational eigenmode emerges at an inflection point in a shell with spatially varying curvature and is responsible for the musicality of the saw. Recent works have reproduced this result using numerical simulations (9, 10), but a deeper understanding of the origin of localization has remained elusive.

A simple demonstration of playing the saw quickly reveals the robustness of its musical quality to imperfections in the saw, irregularities in its shape, and the precise details of how the blade is flexed. Fig. 1*D* shows a time trace and spectrogram of the saw clamped in either a J shape or an S shape (Fig. 1 *B* and *C*) when struck or bowed near the sweet spot. The dull and short-lived sound (Audio 1) associated with the J shape might be contrasted with the nearly pure tone (≈595 Hz) lasting several seconds (Audio 2) when the saw is bowed while shaped like an S. While the pitch can be varied by changing the curvature of the saw, the sustained quality of the note is largely indifferent to the manner of excitation and the specific nature of the clamps, as long as the inflection point is present.

The lack of sensitivity to these details suggests a topological origin for the localized mode responsible for the saw's striking sonority. That topology can have implications for band structures and the presence of edge conducting states even when the bulk is insulating was originally explored in electronic aspects of condensed matter to explain the quantization of the Hall conductance (11) and led to the prediction of topological insulators (12, 13). More recently, similar ideas have been used to understand the topological properties of mechanical excitations, e.g., acoustic and floppy modes in discrete periodic lattices (14–17), in continuum elasticity (18–21), in fluid dynamics in geophysical and active matter systems (22–25), etc. In many of the aforementioned systems, the breaking of time-reversal symmetry leads to the appearance of topologically protected modes. Alternately, in the absence of driven or active elements, spatial symmetries of a unit cell can also be used to achieve topological modes via acoustic analogs of the quantum spin or valley Hall effect (17, 26–29), although these examples rely on carefully engineered periodic lattices. Here we expand the use of topological ideas to continuum shells and show that

Author contributions: L.M. conceived research; S.S., P.B., and L.M. designed research; S.S. and P.B. performed research; S.S., P.B., and L.M. contributed new analytic tools; S.S., P.B., and L.M. analyzed data; and S.S., P.B., and L.M. wrote the paper.

The authors declare no competing interest.

This article is a PNAS Direct Submission. V.V. is a guest editor invited by the Editorial Board.

[1]S.S. and P.B. contributed equally to this work.

[2]To whom correspondence may be addressed. Email: lmahadev@g.harvard.edu.

This article contains supporting information online at https://www.pnas.org/lookup/suppl/doi:10.1073/pnas.2117241119/-/DCSupplemental.

Published April 21, 2022.

underlying the time-reversible Newtonian dynamics of the singing saw is a topological invariant that characterizes the propagation of waves in thin shells, arising from the breaking of up–down inversion symmetry by curvature.

Results

Continuum Model of Thin Shell Dynamics. The saw is modeled as a very thin rectangular elastic shell (thickness $h \ll W < L$, where W, L are the width and length of the strip) made of a material with Young's modulus Y, Poisson ratio ν, and density ρ (Fig. 1*E*). Its geometry is characterized by a spatially varying curvature tensor (second fundamental form) $\mathbf{b}(\mathbf{x})$, where $\mathbf{x} = (x, y)$ is the spatial coordinate in the plane. As the saw is bent only along the (long) x axis, $b_{xx}(x) \equiv b(x)$ is the sole nonvanishing curvature. To describe its dynamical response, we take advantage of its slenderness and treat the saw as a thin elastic shell that can be bent, stretched, sheared, and twisted. Before moving to a computational model that accounts for these modes of deformation as well as real boundary conditions, to gain some insight into the problem and expose the topological nature of elastic waves, it is instructive to instead consider a simplified description valid for shallow shells with slowly varying curvature.

In a thin shallow shell ($h|b_{ij}| \ll 1$), as bending is energetically cheaper than stretching (30), shear becomes negligible ($\mathbf{Q} \approx \mathbf{0}$; Fig. 1*E*), and in-plane deformations propagate much more rapidly (at the speed of sound $c = \sqrt{Y/\rho}$) so that the depth-averaged stresses can be assumed to equilibrated, i.e., $\partial_j \sigma_{ij} = 0$ (6, 31). In this limit, using the solution of these equations in terms of the Airy stress function χ ($\sigma_{ij} = \mathcal{P}_{ij}\nabla^2\chi$, where $\mathcal{P}_{ij} = \delta_{ij} - \partial_i\partial_j/\nabla^2$ is a projection operator; *SI Appendix*, section 3), the in-plane geometric compatibility relation and the linearized dynamical equations for transverse motions can be written as (7, 32)

$$\frac{1}{Yh}\nabla^4\chi = -\mathcal{P}_{ij}\nabla^2(b_{ij}f), \qquad [1]$$

$$\rho h\partial_t^2 f = -\kappa\nabla^4 f + b_{ij}\mathcal{P}_{ij}\nabla^2\chi. \qquad [2]$$

Here f is the out-of-plane deflection of the shell (Fig. 1*E*) and the bending rigidity $\kappa = Yh^3/[12(1-\nu^2)]$. Crucially, in-plane and flexural (out-of-plane) modes remain geometrically coupled in the presence of curvature even in the linearized setting (Eqs. 1 and 2). For a shell bent with constant curvature along the x axis, i.e., a section of a uniform cylinder, $b(x) = b_0$ is a constant. In the bulk of the system, disregarding boundaries, we can Fourier transform Eqs. **1** and **2** using the solution ansatz $f = f_{\mathbf{q}}e^{-i\omega t + i\mathbf{q}\cdot\mathbf{x}}$ to obtain the dispersion relation for flexural waves to be $\omega_\pm(\mathbf{q}) = \pm\sqrt{(\kappa/\rho h)q^4 + c^2 b_0^2 (q_y/q)^4}$ (Fig. 2*A*), where $q = |\mathbf{q}|$. When $q_y = 0$, i.e., the sheet is undeformed in the transverse direction, it remains developable (with generators that run parallel to the y direction), and the bending waves are gapless, i.e., $\omega \to 0$ as $q \to 0$. However, when $q_y \neq 0$, a finite frequency gap $\sim c|b_0|$ (in addition to finite q_y corrections) controlled by the speed of sound and the curvature of the shell emerges as $q \to 0$ (Fig. 2*A*). Intuitively, this arises due to the geometric coupling between bending and stretching deformations in a curved shell which leads to an effective stiffening that forbids wave propagation below a frequency threshold. Similar spectral gaps appear in curved filaments and doubly curved shells as well (31, 33).

For the S-shaped saw, curvature scales of $b \sim 0.4$ to $0.8\ \mathrm{m}^{-1}$ are easily achievable (as in Fig. 1 *B* and *C*), while the typical sound speed in steel is $c \sim 5$ to 6×10^3 m/s so that the frequency gap is of order 2 to 5 kHz. Comparing these estimates to the spectrogram in Fig. 1*D* (further quantified in Fig. 3) suggests that the localized mode excited upon bowing the S-shaped saw (Fig. 1*C*) lies within the frequency gap. The J-shaped saw (Fig. 1*B*) also vibrates at low frequencies (compared to the gap) when struck, presumably through the $q_y = 0$ branch of delocalized flexural modes, although higher frequencies above the band gap can be excited by careful bowing (*SI Appendix*, Fig. S1 *A* and *B*).

Curvature-Induced $\mathbb{Z}_2$ Topological Invariant. To unveil the topological structure of the vibration spectrum of the saw, we cast the second-order dynamical equations (Eqs. **1** and **2**) in terms of first-order equations by taking the square root of the dynamical matrix (14, 34). Focusing on the flexural modes alone, we obtain a Schrödinger-like equation for the transverse deflections of a shallow shell (*SI Appendix*, section 3),

$$\frac{i}{c}\partial_t\Psi = \mathcal{H}\Psi, \quad \mathcal{H} = \begin{pmatrix} 0 & \mathcal{D}^\dagger \\ \mathcal{D} & 0 \end{pmatrix}, \qquad [3]$$

where $\Psi = (c\mathcal{D}^\dagger f,\ i\partial_t f)$ and $\mathcal{D} = i\sqrt{\kappa/Yh}\nabla^2 + b_{ij}\mathcal{P}_{ij}$ and $\dagger$ represents the conjugate transpose. The eigenvalues of the effective Hamiltonian $\mathcal{H}$ are given by the previously derived ($\omega_\pm(\mathbf{q})$), and its complex eigenvectors $\Psi_\pm(\mathbf{q})$ encode the topology of the band structure. The singularities in the arbitrary phase of the eigenvectors signals nontrivial band topology. To understand the phase of eigenvectors along the saw's long direction, we can consider fixing the transverse wave vector $q_y \neq 0$, leading to an effective one-dimensional (1D) system along the x axis. Then the obstruction to continuously define the phase of the eigenvectors at every q_x in Fourier space while respecting all the symmetries of the problem is quantified by the 1D Berry connection $\mathcal{A}(q_x) = i\sum_{n=\pm}\Psi_n(q_x)^\dagger\partial_{q_x}\Psi_n(q_x)$ (the q_y dependence is suppressed) (35, 36). However, what are the symmetries of our elastodynamic system?

One important symmetry is that imposed by classical time-reversal invariance in a passive, reciprocal material ($\mathcal{C} : x \to x$, $t \to -t$, $\Psi \to \Psi^*$; *SI Appendix*, section 3), which maps forward moving waves into backward moving ones and guarantees that eigenmodes appear in complex-conjugate pairs (34). A second symmetry special to the saw is an emergent spatial reflection symmetry in the local tangent plane ($\Pi : x \to -x$, $t \to t$, $\Psi \to \Psi$; *SI Appendix*, section 3), which originates from the uniaxial nature of the prescribed curvature along the x axis and the insensitivity of bending to the orientation of the local tangent plane, a symmetry that is inherited from 3D rotational invariance. The latter is easily seen by noting that the bending energy only involves an even number of gradients via $\nabla^2 f$. Upon simultaneously enforcing both dynamical and spatial symmetries, a new topological obstruction posed by curvature emerges and is quantified by a $\mathbf{Z}_2$ index (*SI Appendix*, section 3),

$$(-1)^\nu = \exp\left[i\int_0^\infty \mathrm{d}q_x\, \mathcal{A}(q_x)\right]\frac{\mathrm{Pf}[\mathbf{W}(0)]}{\mathrm{Pf}[\mathbf{W}(\infty)]}, \qquad [4]$$

similar to topological insulators with crystalline symmetries (37–39). $\mathrm{Pf}[\mathbf{W}]$ denotes the Pfaffian of the antisymmetric overlap matrix $W_{ij}(q_x) = \Psi_i(q_x)^\dagger\mathcal{C}\Pi\Psi_j(q_x)$ ($i, j = \pm$). We note that unlike the mechanical Su–Schrieffer–Heeger chain (14) that exhibits a topological polarization in 1D, the emergent tangent-plane spatial reflection symmetry in our problem forces this polarization to vanish (*SI Appendix*, section 3).

As we work in the continuum, only differences in the topological invariant are well defined independent of microscopic details. Across an interface at which curvature changes sign, i.e., a curvature domain wall, the jump in the topological invariant is given by

$$(-1)^{\Delta\nu} = \mathrm{sgn}(b_< b_>), \qquad [5]$$

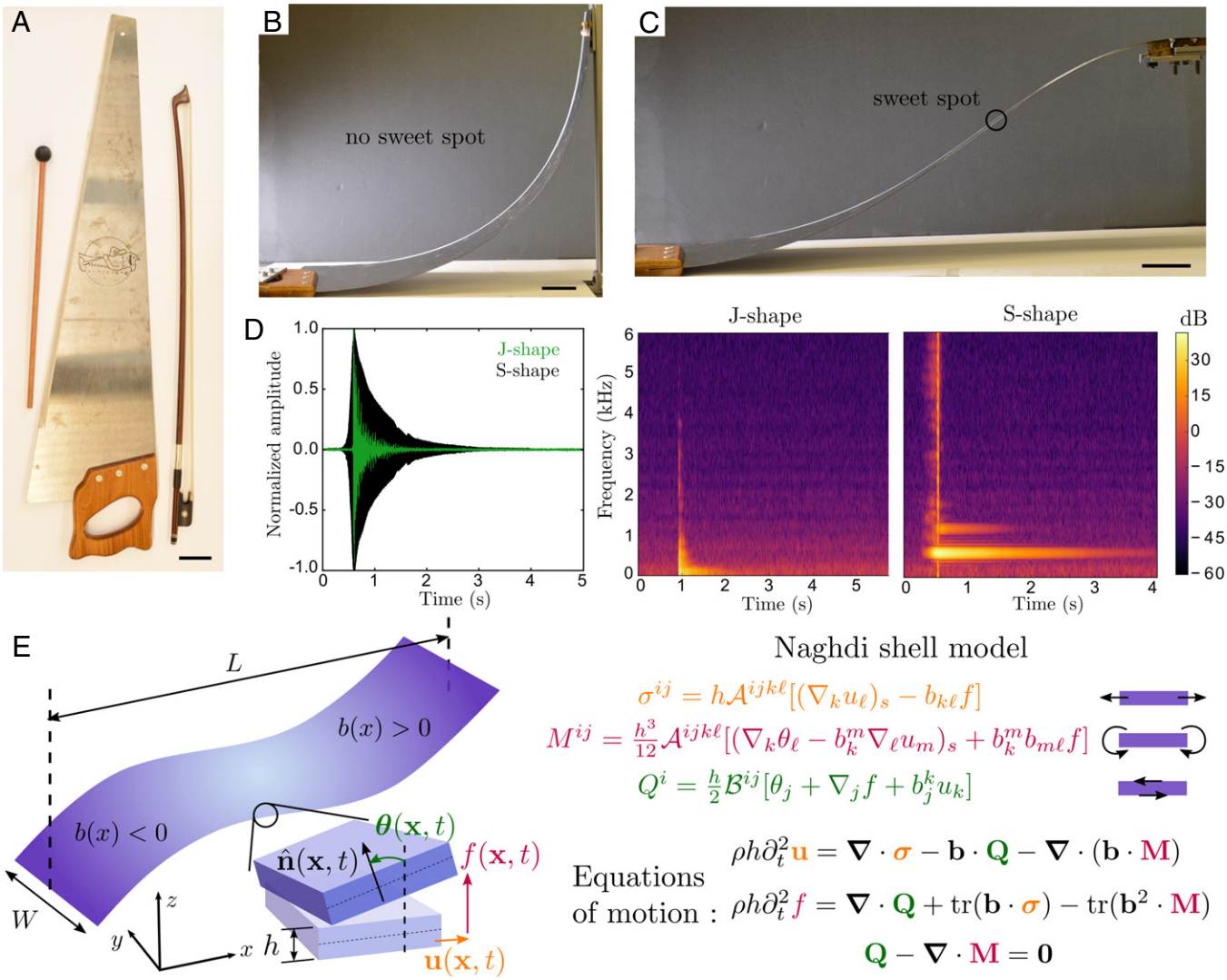

Fig. 1. The musical saw and its mathematical model. (*A*) A violin bow and mallet placed alongside the saw. We clamp the saw in two configurations: (*B*) a J shape and (*C*) an S shape, which is required to play music. The primary distinction between the two is that *C* has an inflection point (the sweet spot) in its profile, while *B* has curvature of constant sign. (Scale bar, 5 cm.) (*D*) (*Left*) Time series of the normalized audio signal when the saw in *B* is struck (green) and when the saw in *C* is bowed (black). (*Middle* and *Right*) The corresponding spectrograms for both the J shape (*B*) and the S shape (*C*). The signal decays rapidly for the J shape with a wider spread in frequency, while for the S shape, a single dominant note with $\omega \approx 595$ Hz survives the ringdown of the blade lasting several seconds. (*E*) A schematic of a blade of length L, width W, and thickness h is sketched with a uniaxial curvature profile $b_{xx}(x) \equiv b(x)$ that changes sign along the x axis as in *B*. The saw can be modeled as an elastic shell whose deformations include an in-plane displacement $\mathbf{u}$, a midsurface deflection f normal to the shell, and a rotation $\boldsymbol{\theta}$ of the local normal $\hat{\mathbf{n}}$ as degrees of freedom [$\mathbf{x} = (x, y)$ is the spatial coordinate]. Elastic tensors $\mathcal{A}^{ijk\ell}$ and $\mathcal{B}^{ij}$ enter the constitutive equations (subscript s denotes symmetrization) for the in-plane stress ($\boldsymbol{\sigma}$), bending moment ($\mathbf{M}$), and transverse shear ($\mathbf{Q}$) (*SI Appendix*, section 2). Derivatives are interpreted as covariant, and index manipulations employ the reference metric of the shell (*SI Appendix*, section 2). The Kirchhoff limit for a shallow shell simplifies the dynamics to $\nabla \cdot \boldsymbol{\sigma} = \mathbf{0}$, $\rho h \partial_t^2 f = \nabla\nabla : \mathbf{M} + \mathrm{tr}(\mathbf{b} \cdot \boldsymbol{\sigma})$, along with $\boldsymbol{\theta} = -\nabla f - \mathbf{b} \cdot \mathbf{u}$ (*SI Appendix*, sections 2 and 3).

where $b_<$ and $b_>$ are the curvature on either side of the interface (*SI Appendix*, section 3). This expression directly demonstrates that the two oppositely curved sections of the saw behave as topologically nontrivial bulk systems, with a $\Delta\nu = 1$, that meet at the inflection line that functions as an internal edge. As a result, nontrivial band topology underlies the emergence of the localized midgap mode, endowing it with robustness against details of the curvature profile and weakly nonlinear deformations (*SI Appendix*, section 3).

Numerical Mode Structure and Localization. We test these predictions by numerically computing the eigenmodes of a finite elastic strip of length $L = 1$ m, width $W = 0.25$ m, and thickness $h = 10^{-3}$ m. For our shell model, we move away from the Kirchhoff model for shells and account for the kinematics associated with shear in addition to those associated with bending and stretching, as they effectively reduce the numerical ill-conditioning commonly seen in high-order continuum theories for slender plates and shells while allowing for numerical methods that require less smoothness and are easier to implement (*SI Appendix*); together, these allow for better computational accuracy. This framework forms the basis for the Naghdi shell model (40) (see *SI Appendix*, section 2, for details) and accounts for an in-plane displacement vector along the midsurface $\mathbf{u}(\mathbf{x}, t)$, an out-of-plane deflection $f(\mathbf{x}, t)$ normal to the shell, and an additional rotation $\boldsymbol{\theta}(\mathbf{x}, t)$ of the local normal itself (Fig. 1*E*). These modes of deformations lead to depth-averaged stress resultants associated with stretching ($\boldsymbol{\sigma}$), bending ($\mathbf{M}$), and shear ($\mathbf{Q}$) as shown in Fig. 1*E*. The resulting covariant nonlinear shell theory along with inertial Newtonian dynamics provides an accurate and computationally tractable description of the elastodynamics of thin shells (Fig. 1*E* and *SI Appendix*, section 2). To highlight the topological robustness of our results, in our calculations we vary both the boundary conditions and curvature profiles imposed on the saw.

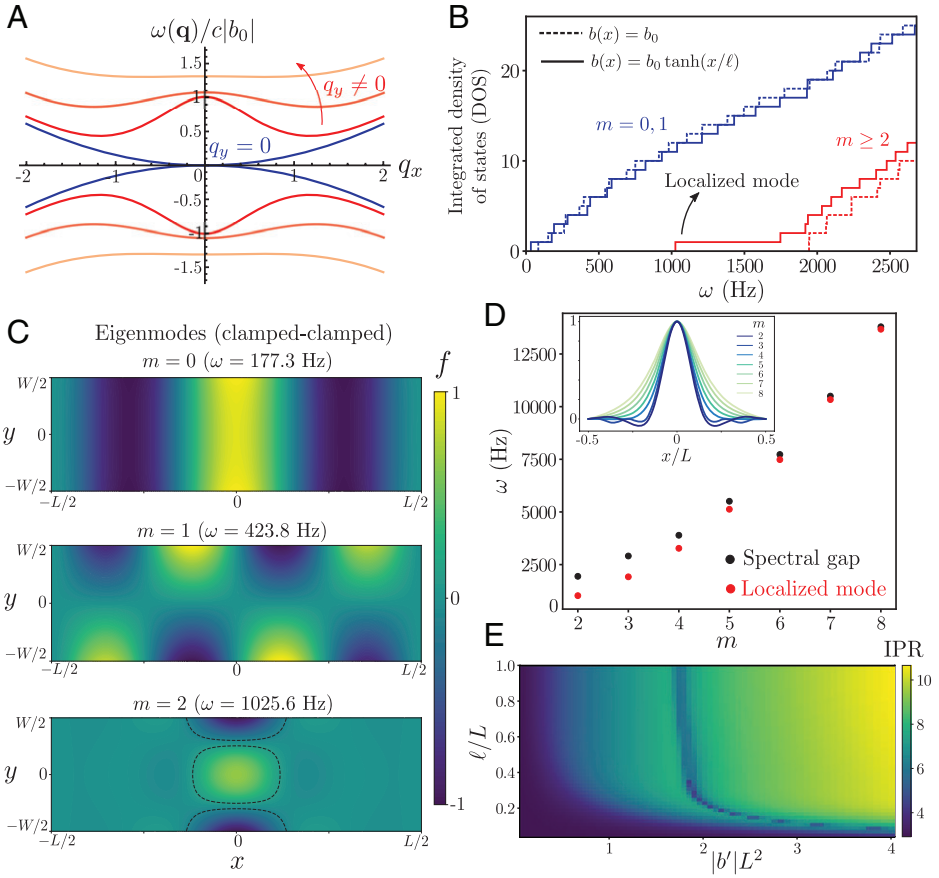

Fig. 2. Eigenmodes, band structure, and topological localization. (*A*) Analytical dispersion relation computed for an infinitely long strip with constant curvature along the x axis ($h|b_0| = 5 \times 10^{-5}$, $\nu = 1/3$). The blue curves correspond to the $q_y = 0$ gapless modes, and the red curves with $q_y \neq 0$ have a finite frequency gap. (*B*) Numerically computed integrated density of states for a finite curved strip ($b_0 L = 0.5$, $\ell/L = 0.1$, $L = 1$ m) with clamped–clamped boundary conditions. Developable eigenmodes (blue; labeled by discrete mode numbers $m = 0, 1$, akin to $q_y = 0$ in the continuum) are gapless for both constant curvature (dashed) and the sigmoid profile (solid). Higher modes (red; $m \geq 2$) exhibit a finite gap ~2 kHz for constant curvature (dashed), while the sigmoid profile features a localized mode ($\omega \sim 1$ kHz) at the inflection point within the bulk band gap. (*C*) Numerical eigenmodes for the sigmoid profile with the local normalized deflection f plotted (dashed lines are 10% isocontours). Low-frequency delocalized states with $m = 0$ (*Top*), $m = 1$ (*Middle,*) and the first localized mode with $m = 2$ (*Bottom*). (*D*) Frequency of the localized modes (*Inset* shows normalized deflection at $y = W/2$ along x) and corresponding spectral gap for increasing transverse mode number $m \geq 2$. (*E*) Inverse participation ratio of the first localized mode for a piecewise linear curvature profile, plotted against the curvature gradient b' and the length scale of curvature variation ℓ.

In Fig. 2*B*, the distribution of eigenmodes as a function of frequency is shown in the integrated density of states for a constant curvature shell, $b(x) = b_0$ (dashed lines), and an S-shaped shell with a smooth curvature profile $b(x) = b_0 \tanh(x/\ell)$ (solid lines) that varies over a width ℓ near the inflection point at $x = 0$ (i.e., a curvature domain wall). In both cases, the ends of the strip are kept clamped, and the spectra are calculated using an open-source code based on the finite element method (41, 42). As the curvature of the S shape approaches a constant $\pm b_0$ far from the origin, the bulk spectral gap and delocalized modes match that of the constant curvature case. Flexural modes that vary at most linearly in the y direction* (labeled by discrete mode numbers $m = 0, 1$ due to the lack of translational invariance) correspond to linearized isometries; they delocalize over the entire ribbon (Fig. 2 *C*, *Top* and *Middle*) and populate states all the way to zero frequency, i.e., with a gapless spectrum. This is true for both constant curvature (dashed blue line, Fig. 2*B*) and the S-shaped shell (solid blue line, Fig. 2*B*) as these bulk modes are unaffected by curvature. In contrast, all other modes that bend in both directions ($m \geq 2$) are generically gapped for a constant curvature profile (dashed red line, Fig. 2*B*) as expected. However, for the S shape, in addition to the gapped bulk modes, a new mode appears within the spectral gap (solid red line, Fig. 2*B*). This midgap state (shown here for $m = 2$) is a localized mode that is trapped in the neighborhood of the inflection line (Fig. 2 *C*, *Bottom*). For increasing mode number $m \geq 2$, similar topological modes appear within the bulk bandgap, with growing localization lengths (Fig. 2 *D*, *Inset*) and higher frequencies (Fig. 2*D*), as predicted analytically (*SI Appendix*, section 3). Qualitatively, the presence of an inflection line in the S-shaped saw makes it geometrically soft there; the generators of cylindrical modes are now along the length of the saw, and the curved regions on either side that are geometrically stiff serve to insulate the soft internal edge from the real clamped edges.

Of particular note is that the localized modes, unlike the extended states, are virtually unaffected by the boundaries and the conditions there (see *SI Appendix*, Fig. S2*A*, for eigenmodes in a strip with asymmetric boundary conditions where the left edge is clamped and the right edge is free). Spatial gradients in curvature, however, do impact the extent of localization. We demonstrate this using a piecewise continuous curvature profile that has a constant linear gradient b' over a length ℓ across the origin and adopts a constant curvature outside this region. By varying both the curvature gradient b' and the length scale ℓ, we can tune the localization of the lowest topological mode (same as Fig. 2 *C*, *Bottom*), quantified by the inverse participation ratio $\mathrm{IPR} = \int \mathrm{d}\mathbf{x}|f(\mathbf{x})|^4 / (\int \mathrm{d}\mathbf{x}|f(\mathbf{x})|^2)^2$ (Fig. 2*E*). Strong localization (high

*Eigenmodes in a finite saw need to vary at least quadratically in y (i.e., $m \geq 2$) in order to couple bending and stretching deformations in the shell.

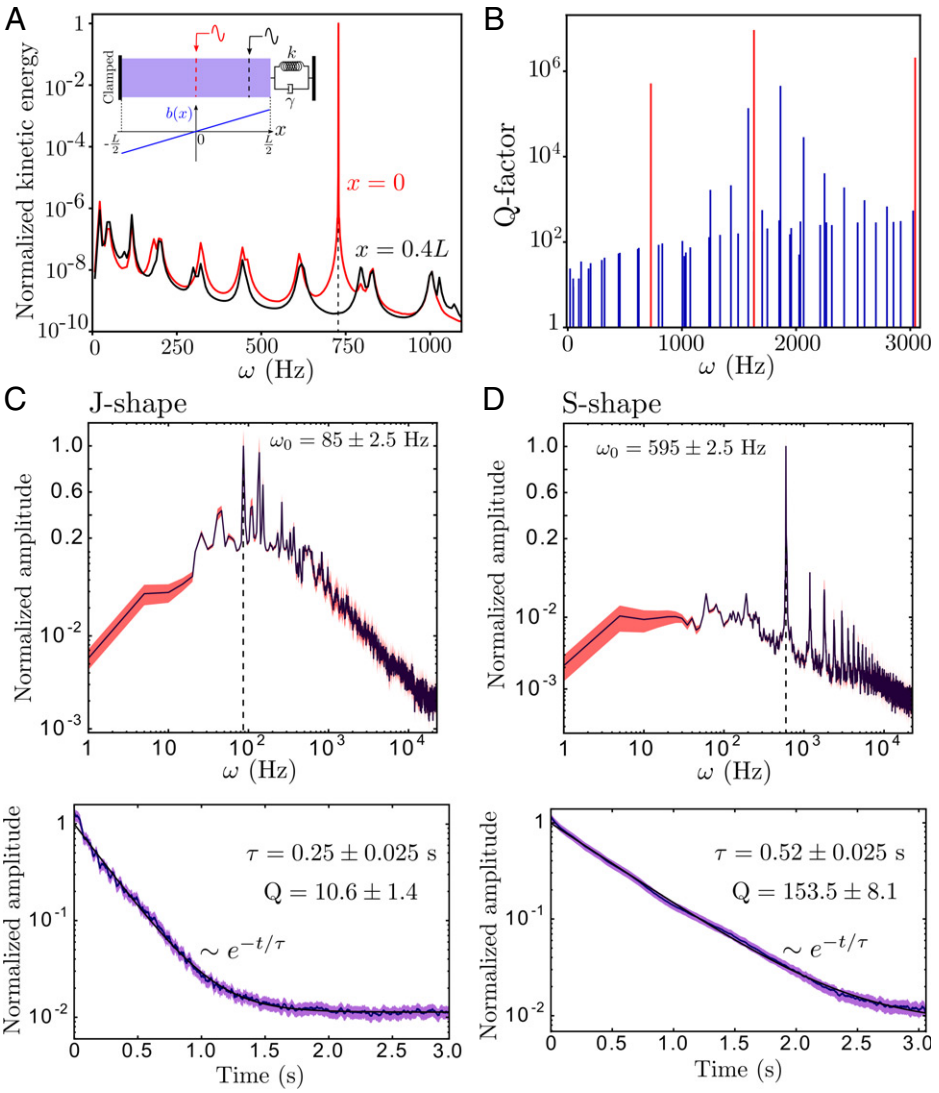

Fig. 3. Dissipative dynamics and high-quality oscillators. (*A*) Resonance curves for a shell with a linear curvature profile (*Inset*) periodically driven at the inflection point ($x = 0$; red) and away from it ($x = 0.4L$; black) for varying frequency ($\omega \approx 740$ Hz corresponds to the first localized mode). (*B*) Numerically computed Q factor shows dramatic enhancement at localized mode frequencies (red) over delocalized modes (blue). (*C* and *D*) Experimental measurement of Q factor (see *SI Appendix*, section 1 for details) for the musical saw in a (*C*) J shape (Fig. 1*B*) and (*D*) S shape (Fig. 1*C*). (*Top*) Note the normalized Fourier spectrum amplitude is on a log scale below 0.1 and linear above, with the peak frequency marked as ω_0. (*Bottom*) The average signal decay (blue curve) is fit to a single decaying exponential (black curve). The shaded region is the SE in both *C* and *D*.

IPR) is quickly achieved for sharp gradients in curvature (IPR $\propto \sqrt{|b'|/h}$; *SI Appendix*, section 3) as long as the length scale of curvature variation is not too small ($\ell/L \geq 0.1$, Fig. 2*E*), corresponding to a diffuse domain wall. In the opposite limit of $\ell \to 0$ for $b'\ell = b_0$ fixed, i.e., a sharp domain wall with a discontinuous curvature profile $b(x) = b_0\,\mathrm{sgn}(x)$, strong localization persists (*SI Appendix*, Fig. S3), consistent with our topological prediction and demonstrating the ease of geometric control of localization.

Geometrically Tunable High-Quality Oscillators. The boundary insensitivity of topologically localized modes has important dynamic consequences that can be harnessed to produce high-quality resonators. The primary mode of dissipation in the saw, as in nanoelectromechanical devices (43), is through substrate or anchoring losses at the boundary. Internal dissipation mechanisms (from, e.g., plasticity, thermoelastic effects, and radiation losses), although present, are considerably weaker and neglected here. To model dissipative dynamics, we retain clamped boundary conditions on the left end and augment the right boundary to include a restoring spring (k) and dissipative friction (γ) for both the in-plane forces and bending moments (Fig. 3 *A*, *Inset*, and *SI Appendix*, section 2). Informed by Fig. 2*E*, we choose a linear curvature profile spanning the entire length of the shell to obtain a strongly localized mode. Upon driving the shell into steady oscillations, with a periodic point force applied at the inflection point ($x = 0$; Fig. 3*A*, red curve), we see an extremely sharp resonance peak right at the frequency of the first localized mode (Fig. 3*A*). In contrast, when the shell is driven closer to the boundary ($x = 0.4L$; Fig. 3*A*, black curve), the response is at least six orders of magnitude weaker as the localized mode is not excited and only the delocalized modes contribute. Localization hence protects the mode from dissipative decay, unlike extended states that dampen rapidly through the boundaries. We further quantify this using a Q factor computed from undriven relaxation of the shell initialized in a given eigenmode (*SI Appendix*, section 2). Ultrahigh values of Q $\approx 10^5$ to 10^6 are easily attained when a localized mode is excited (Fig. 3*B*, red), well over the Q factor of all other modes (Fig. 3*B*, blue). Similar results are obtained for other curvature profiles as well, such as a sigmoid curve (*SI Appendix*, Fig. S2*B*).

To compare these computational results with experiments, we perform ringdown measurements on a musical saw (see *SI Appendix*, section 1, for details) clamped in both the J shape (Fig. 1*B*) and the S shape (Fig. 1*C*). As indicated by Eq. **5**, the key distinguishing feature of the S-shaped saw (compared to the J shape) is the presence of an inflection line (curvature domain wall) that engenders a well-localized domain wall mode capable of sustaining long-lived oscillations. The normalized Fourier spectra and exponential decay (τ) of the signal envelope are shown in Fig. 3*C* (J shape) and Fig. 3*D* (S shape) with the dominant frequency (ω_0) marked. We find a factor $\sim$15 enhancement in the Q factor ($Q = \omega_0\tau/2$) for the S-shaped saw ($Q \approx 150$; Fig. 3 *D*, *Left*) over the J shape ($Q \approx 10$; Fig. 3 *C*, *Left*). We emphasize that this significant quality factor improvement, although not as dramatic as the numerically computed Q factors (Fig. 3*B*), is still striking given the initial impulse (mallet strike for J shape and bow for S shape; see *SI Appendix*, Fig. S1, for other cases) excites an uncontrolled range of frequencies and other sources of energy loss including internal damping are presumably also present.

Discussion and Conclusion

Our combination of analysis, finite element simulations and experiments has demonstrated that a saw sings because its curvature generates a frequency gap in the acoustic spectrum which closes at an inflection point (line) that acts as an interior edge allowing a localized mode to emerge within the band gap. Unlike mechanisms of weak localization (44, 45) or well-known whispering gallery modes (30, 46) that rely sensitively on details of the domain geometry, our topological argument explains the existence of localized sound modes and their robustness against perturbations in the musical saw, providing a framework to explore not just topological mechanics but also dynamics in thin plates and shells.

The ability to control spatial geometry to trap modes at interfaces in the interior of the system offers a unique opportunity to design high-quality oscillators. As our results are material independent, they apply equally well to nanoscale electromechanical resonators (47, 48) and provide a geometric approach to design high-quality resonators without relying on intrinsic nonlinearities (49). Just as in the musical saw, in nanomechanical devices, dissipation can be dominated by radiation through the clamped boundary (43). Current on-chip topological nanoelectromechanical metamaterials use carefully patterned periodic arrays of nanomembranes to control localized modes in robust acoustic waveguides (50, 51). Our work suggests an alternate strategy inspired by the singing saw, which relies solely on the scale separation intrinsic to any curved thin sheet; by manipulating curvature spatially, topological modes localized in the interior hence remain vibrationally isolated and decay extremely slowly, allowing ultrahigh-quality oscillations, perhaps even in the ultimate limit of atomically thin graphene (52).

Materials and Methods

Extended data on the experiments and the details of the numerical modeling and theoretical calculations are provided in *SI Appendix*.

Saw Experiments. The wooden handle of the musical saw (Wentworth) was clamped onto an optical table, while the tapered end of the blade was attached to a sliding metal bracket mounted onto a vertical guide rail. Cork discs (around 2 cm in diameter and 0.5 to 1 cm in thickness) were used to cushion and softly support the clamped end of the blade. This helped damp out oscillations at the saw end and reduced any high-frequency ringing arising from direct metal-on-metal contact. The saw blade was bent into two configurations, a J shape (Fig. 1*B*) and an S shape (Fig. 1*C*), and manually either struck with a mallet or bowed with a violin bow at the straight edge, both near the center of the blade. The blade was allowed to freely ringdown postexcitation. The audio was recorded using a USB microphone (Fifine technology, K669-K669B, sampling frequency $f_s = 44.1$ kHz) placed near the saw and analyzed using the software Audacity.

Multiple measurements of the ringdown signal, each lasting 5 to 6 s, were made with a gap of a few seconds between runs. A separate 10 to 15 s audio sample with a stationary saw was used as a template to filter any background noise using the in-built noise reduction functionality in Audacity. The denoised audio samples were then analyzed using a custom Python code. Both left and right (stereo) channels are strongly correlated with each other, so we simply averaged the two to get the signal for each run. Upon using a Hann window and Fourier transforming each signal, we binned the frequency axis with a bin size of $\Delta\omega = 5$ Hz and averaged the normalized (by the maximum) magnitude of the Fourier transform over different runs ($N = 26$: J shape, mallet; $N = 28$: S shape, bow).

The average spectrum (normalized) is plotted in Fig. 3 *C* and *D*, *Top*, with the shaded region corresponding to the SE over the independent runs. The spectrograms in Fig. 1 *D*, *Middle* and *Right*, were computed for individual audio signals using matplotlib's specgram function with options NFFT = 512 Hz (number of fast Fourier transform data points per block), pad_to = 8, 192 Hz, and noverlap = 256 Hz. In order to compute the decay time of the sound, we normalized each time series by its maximum (in magnitude) and lined them up so $t = 0$ is at the maximum of the signal. We averaged the absolute value of the temporally aligned signals over independent runs and performed an additional moving average over a time step $\Delta t = 0.025$ s to smooth out all the high-frequency oscillations, leaving behind only the required envelope. This smoothed average curve (once again normalized by its maximum) is shown in dark blue in Fig. 3 *C* and *D*, *Bottom*. A similar calculation and smoothing is also done for the SE computed over independent runs and is plotted as the shaded region about the average. The smoothed average time series is then fit to an exponential function with a constant offset using SciPy's in-built nonlinear curve fitting function. The errors on our estimate for the dominant frequency (ω_0) and the decay time (τ) arise primarily from the chosen resolution of our smoothing windows ($\Delta\omega$, Δt) as other sources of measurement error are much smaller. We have nonetheless checked that our choice of the window size ($\Delta\omega$, Δt) is optimum as changing it by small amounts does not affect our results, but decreasing Δt by an order of magnitude significantly degrades the exponential fit.

Data Availability. Code and data reproducing the results in this paper have been deposited on Figshare, https://doi.org/10.6084/m9.figshare.19441385, and are described in the article and supporting information.

ACKNOWLEDGMENTS. S.S. is supported by the Harvard Society of Fellows. S.S. thanks Vincenzo Vitelli for helpful discussions and gratefully acknowledges useful interactions during the virtual 2021 Kavli Institute of Theoretical Physics program "The Physics of Elastic Films: From Biological Membranes to Extreme Mechanics," supported in part by the NSF under Grant NSF PHY-1748958. L.M. acknowledges Grants NSF DMR 2011754 and NSF DMR 1922321, the Simons Foundation, and the Henri Seydoux Fund for partial financial support.

Author affiliations: [a]Department of Physics, Harvard University, Cambridge, MA 02138; [b]Paulson School of Engineering and Applied Sciences, Harvard University, Cambridge, MA 02138; and [c]Department of Organismic and Evolutionary Biology, Harvard University, Cambridge, MA 02138

1. N. H. Fletcher, T. Rossing, *The Physics of Musical Instruments* (Springer New York, 2008).
2. G. Johnson, *Saw, Musical* (Grove Music Online, Oxford University Press, 2001).
3. J. J. Leonard, J. Graebner, *Scratch My Back: A Pictoral History of the Musical Saw and How to Play It.* (Kaleidoscope Press), ed. 1 (1989).
4. R. Cook, Vibration of a segment of a non-circular cylindrical shell: The "musical saw" problem. *J. Sound Vibrat.* **146**, 339–341 (1991).
5. A. Tubis, R. E. Davis, The musical saw-operational features and simple dynamical theory. *J. Acoust. Soc. Am.* **71**, S82–S83 (1982).
6. J. F. M. Scott, J. Woodhouse, Vibration of an elastic strip with varying curvature. *Phil. Trans. R. Soc. A* **339**, 587–625 (1992).
7. W. T. Koiter, "A consistent first approximation in the general theory of thin elastic shells" in *Proceedings of I.U.T.A.M. Symposium on the Theory of Thin Elastic Shells*, W. T. Koiter, Ed. (North-Holland, Amsterdam, 1960), pp. 12–33.

8. B. Audoly, Y. Pomeau, *Elasticity and Geometry: From Hair Curls to the Non-linear Response of Shells* (Oxford University Press, 2010).
9. R. Worland, The musical saw and the flexatone: An experimental study of confined vibrational modes in metal plates of variable curvature. *J. Acoust. Soc. Am.* **139**, 2011–2011 (2016).
10. R. Worland, The musical saw: Musical acoustics of trapped vibrational modes in a curved blade. *J. Acoust. Soc. Am.* **145**, 1750–1750 (2019).
11. D. J. Thouless, M. Kohmoto, M. P. Nightingale, M. den Nijs, Quantized hall conductance in a two-dimensional periodic potential. *Phys. Rev. Lett.* **49**, 405 (1982).
12. M. Z. Hasan, C. L. Kane, Colloquium: Topological insulators. *Rev. Mod. Phys.* **82**, 3045 (2010).
13. X. L. Qi, S. C. Zhang, Topological insulators and superconductors. *Rev. Mod. Phys.* **83**, 1057 (2011).
14. C. Kane, T. Lubensky, Topological boundary modes in isostatic lattices. *Nat. Phys.* **10**, 39–45 (2014).
15. S. D. Huber, Topological mechanics. *Nat. Phys.* **12**, 621–623 (2016).
16. X. Mao, T. C. Lubensky, Maxwell lattices and topological mechanics. *Annu. Rev. Condens. Matter Phys.* **9**, 413–433 (2018).
17. G. Ma, M. Xiao, C. T. Chan, Topological phases in acoustic and mechanical systems. *Nat. Rev. Phys* **1**, 281–294 (2019).
18. D. Bartolo, D. Carpentier, Topological elasticity of nonorientable ribbons. *Phys. Rev. X* **9**, 041058 (2019).
19. A. Saremi, Z. Rocklin, Topological elasticity of flexible structures. *Phys. Rev. X* **10**, 011052 (2020).
20. K. Sun, X. Mao, Continuum theory for topological edge soft modes. *Phys. Rev. Lett.* **124**, 207601 (2020).
21. K. Sun, X. Mao, Fractional excitations in non-Euclidean elastic plates. *Phys. Rev. Lett.* **127**, 098001 (2021).
22. P. Delplace, J. B. Marston, A. Venaille, Topological origin of equatorial waves. *Science* **358**, 1075–1077 (2017).
23. S. Shankar, M. J. Bowick, M. C. Marchetti, Topological sound and flocking on curved surfaces. *Phys. Rev. X* **7**, 031039 (2017).
24. A. Souslov, K. Dasbiswas, M. Fruchart, S. Vaikuntanathan, V. Vitelli, Topological waves in fluids with odd viscosity. *Phys. Rev. Lett.* **122**, 128001 (2019).
25. S. Shankar, A. Souslov, M. J. Bowick, M. C. Marchetti, V. Vitelli, Topological active matter. arXiv [Preprint] (2020). https://arxiv.org/abs/2010.00364 (Accessed 7 April 2022).
26. R. Süsstrunk, S. D. Huber, Observation of phononic helical edge states in a mechanical topological insulator. *Science* **349**, 47–50 (2015).
27. M. Miniaci, R. Pal, B. Morvan, M. Ruzzene, Experimental observation of topologically protected helical edge modes in patterned elastic plates. *Phys. Rev. X* **8**, 031074 (2018).
28. R. K. Pal, M. Ruzzene, Edge waves in plates with resonators: An elastic analogue of the quantum valley hall effect. *New J. Phys.* **19**, 025001 (2017).
29. H. Nassar *et al.*, Nonreciprocity in acoustic and elastic materials. *Nat. Rev. Mater.* **5**, 667–685 (2020).
30. J. W. S. B. Rayleigh, *The Theory of Sound* (Macmillan, 1896), vol. 2.
31. A. A. Evans, A. J. Levine, Reflection and refraction of flexural waves at geometric boundaries. *Phys. Rev. Lett.* **111**, 038101 (2013).
32. P. G. Ciarlet, *Theory of Shells, Mathematical Elasticity.* (Elsevier Science, 2000).
33. J. Kernes, A. J. Levine, Effects of curvature on the propagation of undulatory waves in lower dimensional elastic materials. *Phys. Rev. E* **103**, 013002 (2021).
34. R. Süsstrunk, S. D. Huber, Classification of topological phonons in linear mechanical metamaterials. *Proc. Natl. Acad. Sci. U.S.A.* **113**, E4767–E4775 (2016).
35. T. Frankel, *The Geometry of Physics: An introduction* (Cambridge University Press, 2011).
36. M. Nakahara, *Geometry, Topology and Physics* (CRC Press, 2018).
37. L. Fu, C. L. Kane, Topological insulators with inversion symmetry. *Phys. Rev. B Condens. Matter Mater. Phys.* **76**, 045302 (2007).
38. L. Fu, Topological crystalline insulators. *Phys. Rev. Lett.* **106**, 106802 (2011).
39. T. L. Hughes, E. Prodan, B. A. Bernevig, Inversion-symmetric topological insulators. *Phys. Rev. B Condens. Matter Mater. Phys.* **83**, 245132 (2011).
40. P. M. Naghdi, "Foundations of elastic shell theory" in *Progress in Solid Mechanics*, I. N. Sneddon, R. Hill, Eds. (North-Holland, Amsterdam, 1963), vol. 4, pp. 1–90.
41. M. S. Alnæs *et al.*, The FEniCS project version 1.5. *Arch. Numer. Softw.* **3**, 9–23 (2015).
42. J. S. Hale, M. Brunetti, S. P. A. Bordas, C. Maurini, Simple and extensible plate and shell finite element models through automatic code generation tools. *Comput. Struc.* **209**, 163–181 (2018).
43. I. Wilson-Rae *et al.*, High-Q nanomechanics via destructive interference of elastic waves. *Phys. Rev. Lett.* **106**, 047205 (2011).
44. S. M. Heilman, R. S. Strichartz, Localized eigenfunctions: Here you see them, there you don't. *Not. Am. Math. Soc.* **57**, 624–629 (2010).
45. M. Filoche, S. Mayboroda, Universal mechanism for Anderson and weak localization. *Proc. Natl. Acad. Sci. U.S.A.* **109**, 14761–14766 (2012).
46. L. Rayleigh, Cxii. The problem of the whispering gallery. *Lond. Edinb. Dublin Philos. Mag. J. Sci.* **20**, 1001–1004 (1910).
47. H. G. Craighead, Nanoelectromechanical systems. *Science* **290**, 1532–1536 (2000).
48. K. L. Ekinci, Electromechanical transducers at the nanoscale: Actuation and sensing of motion in nanoelectromechanical systems (NEMS). *Small* **1**, 786–797 (2005).
49. R Lifshitz, M. C. Cross, "Nonlinear dynamics of nanomechanical and micromechanical resonators" in *Review of Nonlinear Dynamics Complexity*, H. G. Schuster, Ed. (Wiley, 2008), pp. 1–48.
50. J. Cha, K. W. Kim, C. Daraio, Experimental realization of on-chip topological nanoelectromechanical metamaterials. *Nature* **564**, 229–233 (2018).
51. J. Ma, X. Xi, Y. Li, X. Sun, Nanomechanical topological insulators with an auxiliary orbital degree of freedom. *Nat. Nanotechnol.* **16**, 576–583 (2021).
52. J. S. Bunch *et al.*, Electromechanical resonators from graphene sheets. *Science* **315**, 490–493 (2007).